ACS Catalysis

pubs.acs.org/acscatalysis

Research Article

Modeling the Potential-Dependent Kinetics of CO_2 Electroreduction on Single-Nickel Atom Catalysts with Explicit Solvation

Hongyan Zhao, Hao Cao, Zisheng Zhang, and Yang-Gang Wang*

Cite This: *ACS Catal.* 2022, 12, 11380−11390

Read Online

ACCESS | Metrics & More | Article Recommendations | Supporting Information

ABSTRACT: Single-metal atom catalysts in nitrogen-doped graphene supports have attracted growing attention as state-of-the-art CO_2 reduction reaction (CO_2RR) electrocatalysts. Nevertheless, theoretical explorations on such systems remain immensely insufficient owing to the complexity in realistic modeling of the solid/liquid interface and the lack of understanding of the potential dependence of the reaction mechanisms and the catalytic nature of active sites. In this work, we develop a methodology of Langmuir adsorption model-derived potential-dependent kinetics (LPD-K) to probe the potential-dependent kinetics of the CO_2RR on single-atom electrocatalysts. Using this LPD-K method, we show how to predict the potential-dependent chemistry using a specific example, single-nickel atom nitrogen−graphene catalysts (NiN_nC_{4-n}@Gra, n = 1−4). We investigate the reaction mechanisms and energetics at the electrochemical interface using *ab initio* molecular dynamics (AIMD) simulations with fully explicit solvation, in conjunction with thermodynamic integration methods and electrode potential analysis. The effect of the applied electrode potential on the free energetics of the CO_2RR on NiN_nC_{4-n}@Gra is comprehensively discussed. It is suggested that both reaction energies and barriers for CO_2 adsorption and further protonation are approximately linearly correlated with the applied electrode potentials but the slopes are distinctly deviated from 1 eV per volt. Based on the correlations of potential-dependent free energetics and the proposed kinetic model, we predict the onset potentials of the CO_2RR under both basic and acidic conditions, which are comparable with the experimental observations. In addition, our findings reveal the structural impact of the catalytic activity of a single-Ni atom catalyst with different coordination environments. In a broad sense, probing the structural origin and thermodynamic CO_2RR analysis could inspire the rational design of efficient MNC@Gra-based CO_2RR catalysts.

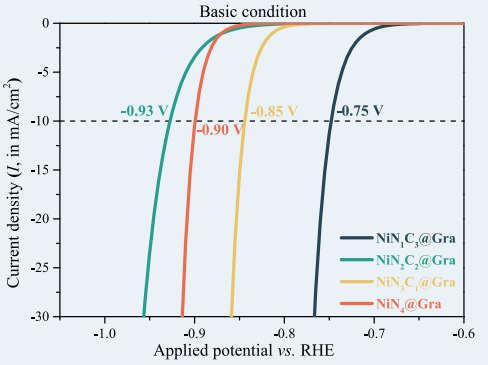

KEYWORDS: *ab initio molecular dynamics, thermodynamic integration, single-atom catalysis, CO_2 electroreduction, potential-dependent reaction free energy*

INTRODUCTION

Electrocatalysis of the CO_2 reduction reaction (CO_2RR) to CO is a promising effective method to mitigate the severe CO_2 concentration in the atmosphere and achieve the goal of converting CO_2 into renewable feedstock and sustainable energies.[1−5] To this end, numerous electrocatalysts[6] have been extensively investigated for an efficient CO_2RR, among which the state-of-the-art single-atom catalysts (SACs) characterized by atomically dispersed metal atoms on suitable substrates have become cutting-edge catalysts since they were first proposed in 2011.[7] Thereinto, nickel atoms embedded in nitrogen-anchored graphene (NiN_nC_{4-n}@Gra), which possess distinguished reactivity and selectivity for the CO_2RR to CO in the aqueous phase, have received much attention because of the impressive Faradaic efficiencies for the CO_2RR.[8−12] However, the structural catalytic nature and reaction mechanism remain controversial, and there is a substantial divergence about the rate-determining step (RDS) in recent investigations, although it seems apparently simple. For instance, preceding reports put forward the RDS to be CO_2 adsorption on Au,[13,14] Ni- and Fe-embedded MNC catalysts (NiN_nC_{4-n}@Gra and FeN_4C@Gra),[15,16] CO_2(g) to *COOH on noble metals,[17,18] or the *COOH to CO(g) step on Ag from C−O bond cleavage.[19] Additionally, no effort had been spared to study the reactivity and identity of the CO_2RR on NiN_nC_{4-n}@Gra limited exclusively in an alkaline electrolyzer experimentally and theoretically in past decades.[20−24] However, for all that, experimental evidence demonstrated that NiN_4@Gra features high catalytic performance, which even rival Au- and Ag-based catalysts in acidic medium.[10,12] In addition, theoretical explorations on such systems remain immensely insufficient owing to the complexity in realistic modeling of the solid/liquid interface and the lack of

Received: May 14, 2022
Revised: August 4, 2022
Published: September 5, 2022

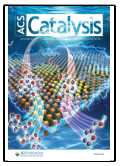

https://doi.org/10.1021/acscatal.2c02383
ACS Catal. 2022, 12, 11380−11390

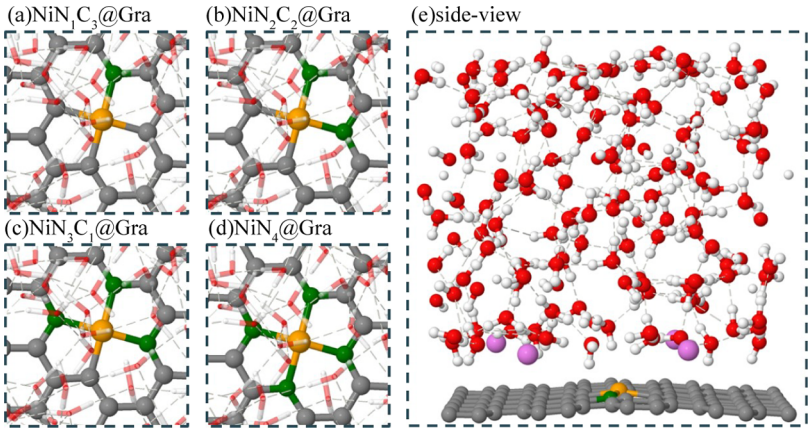

Figure 1. (a–d) Top view of different atomic configurations in the graphene matrix for nitrogen-anchored graphene on coordination. (e) Side view of the simulation models of NiN_1C_3@Gra. Hydrogen bonds are depicted by thin dashed lines. The nickel, carbon, nitrogen, oxygen, hydrogen, and sodium atoms are colored in orange, gray, green, red, white, and pink, respectively.

understanding of the potential dependence of the reaction mechanisms and the catalytic nature of active sites. In this sense, it is essential to explore the catalytic reactivity and selectivity of the CO_2RR over the NiN_nC_{4-n}@Gra electrode due to the lack of theoretical data.

Even though the well-developed computational hydrogen electrode (CHE)[25] model has been widely adopted in past years, some realistic conditions, such as external applied potential[26] and electric field effects,[20] need to be taken into consideration. Even so, many theoretical trials have been devoted to exploring models by introducing extra electrons into the system.[20,23,27] Nevertheless, nowadays, instead of bringing in redundant charge, counterions are more extensively employed in the establishment of electric field to adjust the applied potential and elucidate the solid/liquid interface liquid structure.[28,29] Le et al. explored the Helmholtz layer of electrified solid/liquid interfaces by introducing Na atoms into the Pt(111)/water interface and demonstrated that it is a good approach to describe the potential and probe electrocatalysis processes.[29] Thus, in this work, by utilizing the well-adopted methodology of workfunction tuning by introducing Na^+ counterions, with a sufficiently thick explicit water layer, the mechanism of the catalytic CO_2RR in an aqueous environment over the NiN_nC_{4-n}@Gra electrode/electrolyte interface and the corresponding reaction kinetics are systematically investigated by combining *ab initio* molecular dynamics (AIMD), constrained MD, and thermodynamic integration.

We noticed that many theoretical developments investigate the details of CO_2RR mechanisms and mainly focus qualitatively on the reactivity and selectively of the CO_2RR.[21] As the examples given in the literature, Li et al. addressed that the reactivity of NiN_4@Gra excelling that of N@Gra (only N doped) toward the CO_2RR is based on the observed thermodynamics of the RDS without considering the electrolyte and voltage impact.[21] Herein, we attempt to quantify the effect of the potential-dependent reaction barrier on the CO_2RR activity to shed light and rationalize the catalytic behavior. Particularly, we will give the Langmuir adsorption model-derived potential-dependent kinetics (LPD-K) from traditional fixed-electron-based free energies and barriers, which we believe will favor the investigation of the catalytic behavior of SAC with widespread application and promotion. To concretize the concepts underlying this theoretical methodology, here, we narrate the application of LPD-K to predict the detailed reaction mechanism and rates for the CO_2RR over NiN_nC_{4-n}@Gra electrodes. Through applying our constructed LPD-K model and analyzing reaction barriers and charge transfer, we report the potential-dependent kinetics of the CO_2RR on these catalysts and predict the onset potentials, which are comparable with experimental observations.[9,21,24,30] In addition, we show that the effective surface charge density is the key factor that drives the charge transfer to CO_2 during the CO_2RR on NiN_nC_{4-n}@Gra.

METHODS

Static Calculations and Computational Models. All static calculations are performed using spin-polarized density functional theory (DFT) with the Perdew–Burke–Ernzerhof (PBE) functional[31] based on the Vienna *ab initio* simulation package (VASP).[32,33] The plane-wave basis set cutoff is at 400 eV, and the generalized gradient approximations (GGA)[34] is used to describe the exchange-correlation energy, while projector augmented wave (PAW)[35] is used to describe core electrons. The supercell is constructed by orthogonalized 6 × 4 unit cells of graphene with dimensions of 17.04 × 14.76 × 20.00 $Å^3$. Two adjacent C atoms are removed to construct a divacancy to load the single nickel atom, which is coordinated to 1–4 nitrogen/carbon atoms through strong covalent bonds, denoted as NiN_1C_3@Gra, NiN_2C_2@Gra, NiN_3C_1@Gra, and NiN_4@Gra (Figure 1a–d). Raman and transmission electron microscopy (TEM) characterizations evidenced that predoped N plays an indispensable role in creating defects on graphene shells, which assist in trapping and bonding a significant number of Ni atoms in the graphene shells.[36–38] We have also calculated formation energies to explore the stability of these catalysts, Table S1. It is suggested that the single-Ni atom catalyst is less stable with a lower N content and the NiN4@Gra catalyst is the most energetically favorable one. Therefore, we have not considered the single-Ni atom catalyst without doping N in this work, although our free energetic simulations indeed imply that the lower N content should result in high activity for the CO_2RR. Herein, we considered the four possible structures to identify the correlation between the coordination environment and catalytic performance of the CO_2RR in the atomic scale and help the rational design of nanostructured catalysts,[39,40] in addition to tackle the dispute of the experimental observations of the structural information.[9,21]

https://doi.org/10.1021/acscatal.2c02383
ACS Catal. 2022, 12, 11380–11390

In our simulation model, we placed 141 water molecules, leading to the average density of ∼1 g·cm^{-3} to model the solvent water environment. The corresponding equilibrated structures obtained from the 5 ps AIMD simulation are presented in Figure 1e. The three-dimensional periodic boundary condition is applied to the supercell, giving rise to water molecules surrounding both the sides of the graphene surfaces.

***Ab Initio* Molecular Dynamics (AIMD) Calculations and Free Energy Sampling.** All molecular dynamics simulations are carried out using the Quickstep module with the CP2K package[41] because of its quick simulation speed with plenteous explicit solvent water molecules. The core electrons of Ni, C, N, O, H, and Na atoms are represented by the Goedecker−Teter−Hutter (GTH)-type pseudopotentials,[42,43] while their valence orbitals are expanded in the Gaussian and auxiliary plane-wave (GPW)-type double-ζ basis sets[44] with one set of polarization functions (DZVP)[45] with a plane wave cutoff for density expansion of 400 Ry. The PBE functional[31] is utilized to determine the electron exchange and correlation energies, with the Grimme D3 dispersion corrections.[46] During the AIMD simulation, the self-consistent field convergence criterion is set to 10^{-5} Ry for both the electronic gradients and total energies. To get the longer timestep of 1 fs, the deuterium mass of 2.0 is employed for all hydrogen atoms in AIMD runs. Unless otherwise specified, these MD simulations are set to 10 ps under a canonical ensemble (NVT), in which the temperature is controlled at 300 K using Nosé−Hoover thermostats.[47,48]

In order to evaluate the reaction dynamics, free energy profiles are provided from the integration of the potential of mean force (PMF) with respect to the suitable predefined collective variables (CVs) used as reaction coordinates,[49] and the details of the method can be referred to in the literature.[50,51] In this method, we obtained $\frac{dA}{d\xi} = \left\langle \frac{\delta H_\xi^F}{\delta \xi} \right\rangle$ by taking the derivative of the free energy $A(\xi)$ with regard to the reaction coordinate ξ, where H_ξ^F is the Fixman Hamiltonian of the generalized coordinates. The derivative of the Hamiltonian against ξ corresponds to an external force applied to the studied system to retain the reaction coordinates fixed. In our systems, taking the CO_2 activation step as an example, the change of the Hamiltonian with respect to ξ is denoted by the SHAKE Lagrange multiplier λ for constraining the C−Ni distances, which is the characteristic variable between the initial state (IS) and the final state (FS) (Figure 2a). As a result, we perform a succession of constrained MD calculations

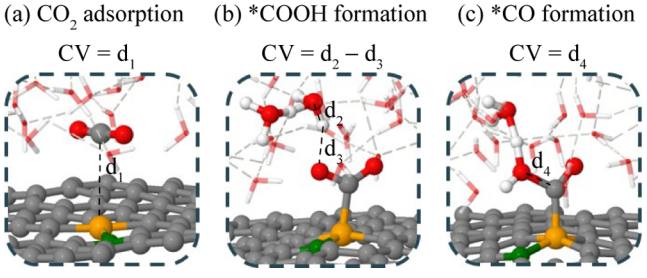

Figure 2. Schematic illustration of collective variables (CVs) used as reaction coordinates in the constrained MD approach, for the reaction of (a) CO_2 adsorption, (b) *COOH formation, and (c) *CO formation.

to obtain the mean force for the set of C−Ni distances along the reaction coordinate from IS [CO_2 (gas phase)] to FS [*CO_2, adsorbed on NiN_nC_{4-n}@Gra]. In the force−distance curves, the three zero-force points correspond to the initial, transition, and final states. The free energy profiles can then be obtained by integrating the average forces with respect to the C−Ni distance. For the *COOH formation reaction, the reaction coordinate is defined as combined CV depicted in Figure 2b, while for the *CO-OH dissociation step, the C−O bond length is the most distinguished choice for CV (Figure 2c). In each constrained MD run, the trajectories of the initial 5 ps are used to equilibrate the systems, followed by another 5 ps remainder of production periods to converge into one mean force for data collection.

Description of the Electrode Potential. The essential part of this communication is simulating the electrochemical reaction energetics infinitely close to the practical environment, which requires us to introduce the electrode potential properly. In the past few decades, many studies have reported that the surface charge density, σ, is one of the most suitable approaches of electric double layers (EDLs) on reaction kinetics,[26,52] since it models the electrochemical interface properly and it does not rely on simulation cell size or predicted interfacial capacitance. Here, we involve the electrode potential-dependent reaction kinetics with σ-dependent kinetics through the following equation

$$\phi = \frac{1}{C}\sigma + \phi_{pzc}$$

where for pristine graphene, experimental interfacial capacitance, C, of 21 μF·cm^{-2}[53] and potential of zero charge, ϕ_{pzc}, of −0.07 V[54] are adopted. We note that we have assumed that the capacitance of the graphene remains unchanged under different potentials, which may result in a systematic shift in the estimated potentials, while the major methodologies and conclusions presented in this work should still quantitatively maintain reliability.

We employ the average value of the potentials at the initial state (U_{IS}) and final state (U_{FS}) as the potential (U_r) of the reaction. (i.e., $U_r = (U_{IS} + U_{FS})/2$).[55] The detailed electrode potentials, surface charges, and corresponding correction terms for each free energy profile are provided in Table S3. In our simulation models, the EDLs at the electrode/electrolyte interfaces are varied by introducing different numbers of alkali Na cations at ∼3 Å (Stern layer) away from the graphene surface (Figure 1e). Because the global system is charge-neutral, the presence of Na^+ would induce excess electrons to aggregate at the graphene surface concurrently and form the EDLs. σ is determined by the number of Na^+ immersed in the model. In fact, it should be noted that the electrode potential of the system changed evidently during the reduction process, which can be ascribed to the charge deviations of the electrode surface within the small cell size of the simulation model.[56,57] However, the influence of such a variation on the reaction free energy is found to be minimal (Table S3); to streamline the calculation, we ignored the electrode potential shift during the process, even though it is contradictory to the practical electrocatalytic environment under constant potentials. It has remained a challenging task to obtain an accurate free energy profile at a constant potential, i.e., performing sufficiently sampling for both the configurational entropy and electronic contributions within the grand canonical ensemble (of electrons). In this work, each constrained MD simulation is

https://doi.org/10.1021/acscatal.2c02383
ACS Catal. 2022, 12, 11380−11390

performed within the canonical ensemble with a constant charge, which inevitably comes with a shift in the workfunction along the reaction coordinate. However, the influence of such a shift on the reaction free energy has been tested to be minimal and does not affect any of the major conclusions for the current study.

Kinetic Model of the CO_2RR. In this section, we propose a kinetic model to explore the potential-dependent kinetics of the CO_2RR on the single-nickel atom catalysts. In general, many previous calculations have shown that the rate-determining step for the CO_2RR to CO is the first hydrogenation step.[11,21,22,58] Therefore, we herein only calculate the reaction rate based on the first hydrogenation step, which is decoupled to be two elementary steps, CO_2 adsorption (i.e., the electron transfer step) and the proton transfer step in our study. The adsorption step can be expressed as $CO_2 + * \leftrightarrow *CO_2^{\delta-}$, and the proton transfer step can be expressed as $*CO_2^{\delta-} + H^+ \rightarrow *COOH$ under acidic conditions or $*CO_2^{\delta-} + H_2O \rightarrow *COOH + OH^-$ under basic conditions, where * denotes the active site (i.e., the single-atom site) and $*CO_2^{\delta-}$ denotes the adsorbed CO_2 species with an electron.

We assume that CO_2 adsorption should experience an adsorption/desorption equilibrium prior to the following hydrogenation steps, and the coverage of $*CO_2^{\delta-}$ on the active site is significant to the actual current density, since it is the main electron transfer step. The coverage of the adsorbed CO_2 is determined by the applied potential and can be obtained by the equilibrium constant. For the adsorption step, $CO_2 + * \leftrightarrow *CO_2^{\delta-}$, the equilibrium equation is expressed as

$$K = \frac{\theta_{*CO_2}}{a_{CO_2(aq)} \times \theta_{(*)}} = \frac{\theta_{*CO_2}}{f\frac{P_{CO_2}}{P^{\circ}} \times (1 - \theta_{*CO_2})} \quad (1)$$

where K is the adsorption equilibrium constant; θ_{*CO_2} is the equilibrated coverage of $*CO_2$ species; θ_* is the coverage of the unoccupied active site; and $a_{CO_2(aq)}$ is defined as the activity of gas CO_2 in the aqueous phase. In the gas phase, the activity of gaseous CO_2 is usually considered to be its pressure; however, it is hard to decide the accurate value of $a_{CO_2(aq)}$ in the aqueous phase. We therefore introduce a constant f as the activity coefficient for CO_2 in the aqueous phase in our model. This constant can be considered as the contribution of the solvent effect on the gas-phase CO_2. This value is assumed to be the same for the catalysts reported in this study. We also note that K is potential-dependent and can be calculated according to the potential-dependent adsorption free energy change $\Delta G_{ads}(U)$

$$K(U) = \exp(-\frac{\Delta G_{ads}(U)}{RT}) \quad (2)$$

From eq 1, we could obtain the equilibrated coverage of $*CO_2$ species

$$\theta_{*CO_2} = \frac{Kf\frac{P_{CO_2}}{P^{\circ}}}{1 + Kf\frac{P_{CO_2}}{P^{\circ}}} \quad (3)$$

From eq 3, one could conclude that in our model, we in fact assume the adsorption of CO_2 as a Langmuir adsorption model and the equilibrated coverage obeys a revised equation for the Langmuir Isotherm.

With the equilibrated coverage being obtained, the reaction rate under the basic conditions can be simply calculated as

$$r = k_p \times \theta_{*CO_2} = \frac{k_B T}{h}\exp\left(-\frac{\Delta G_p^{\#}(U)}{k_B T}\right) \times \theta_{*CO_2} \quad (4)$$

where k_p and $\Delta G_p^{\#}(U)$ are the rate constant and the free energy barrier for the proton transfer step, respectively. We note that the activity of the proton (either in the form of a hydronium ion or water) in the rate equation is set to 1 by assuming that water can always directly approach the active site in the aqueous phase under basic conditions or the concentration of the hydronium ion as 1 mol/L. Based on eq 3, we could arrive at an expression for the total current calculation[23]

$$I = nq_e\rho_{Ni}r = nq_e\rho_{Ni} \times \frac{k_B T}{h}\exp\left(-\frac{\Delta G_p^{\#}(U)}{k_B T}\right) \times \theta_{*CO_2} \quad (5)$$

in which I is the current density, n is the number of transferred electrons ($n = 2$ is adopted for the CO_2RR to CO), *and* q_e, k_B, h, and ρ_{Ni} are the charge of an electron, Boltzmann constant, Planck's constant, and the density of the single-atom site, respectively.

We note that the quasi-equilibrium approximation is basically reasonable under basic conditions (usually the experimental condition) as the free barrier of the protonation step is at least 0.3 eV higher than that in the CO_2 step for $U < -0.6$V based on our calculations. For acidic conditions, the proton originates from the hydronium ion and protonation becomes much easier; it is still a rough approximation for estimating the onset potentials, since the desorption barrier of CO_2 is relatively lower than that of protonation under low potentials. We also neglect the coverage of COOH and CO by assuming that CO is quickly formed by the conversion of COOH and desorbs from the active site due to the low product pressure of CO. HER is also not considered in our kinetic model, considering that hydrogen adsorption is found less favorbale than CO_2 adsorption under the applied potentials on single Ni catalysts. Therefore, the current LPD-K method is a very simple kinetic model that only considers the first hydrogenation step. More accurate kinetic simulations could be achieved by performing microkinetic simulations with all the elementary steps taken into consideration, which need a high computational cost for the potential-dependent free energy estimations using constrained MD simulations.

RESULTS AND DISCUSSION

Potential-Dependent Free Energy Profile. We first studied the free energy profiles of the CO_2RR on a single-nickel atom catalyst under basic and acidic conditions to explore the potential dependence of the activity, since recent experimental studies have shown that the reaction can take place not only in basic solutions[20−24] but also in weakly acidic electrolytes and displays high electrocatalytic CO_2RR performance and CO formation selectivity[10,12] (with a FE of over 90%). The generally accepted reaction mechanism for the CO_2RR to CO on single-nickel atom catalyst (NiN_nC_{4-n}@Gra) electrodes consists of the three following steps: (i) adsorption of CO_2, (ii) protonation of the adsorbed CO_2 to form the COOH intermediate, and (iii) splitting of COOH to produce CO; the latter two are considered to be proton-coupled electron transfer (PCET) steps.[10−12] Figure 3 presents

https://doi.org/10.1021/acscatal.2c02383
ACS Catal. 2022, 12, 11380−11390

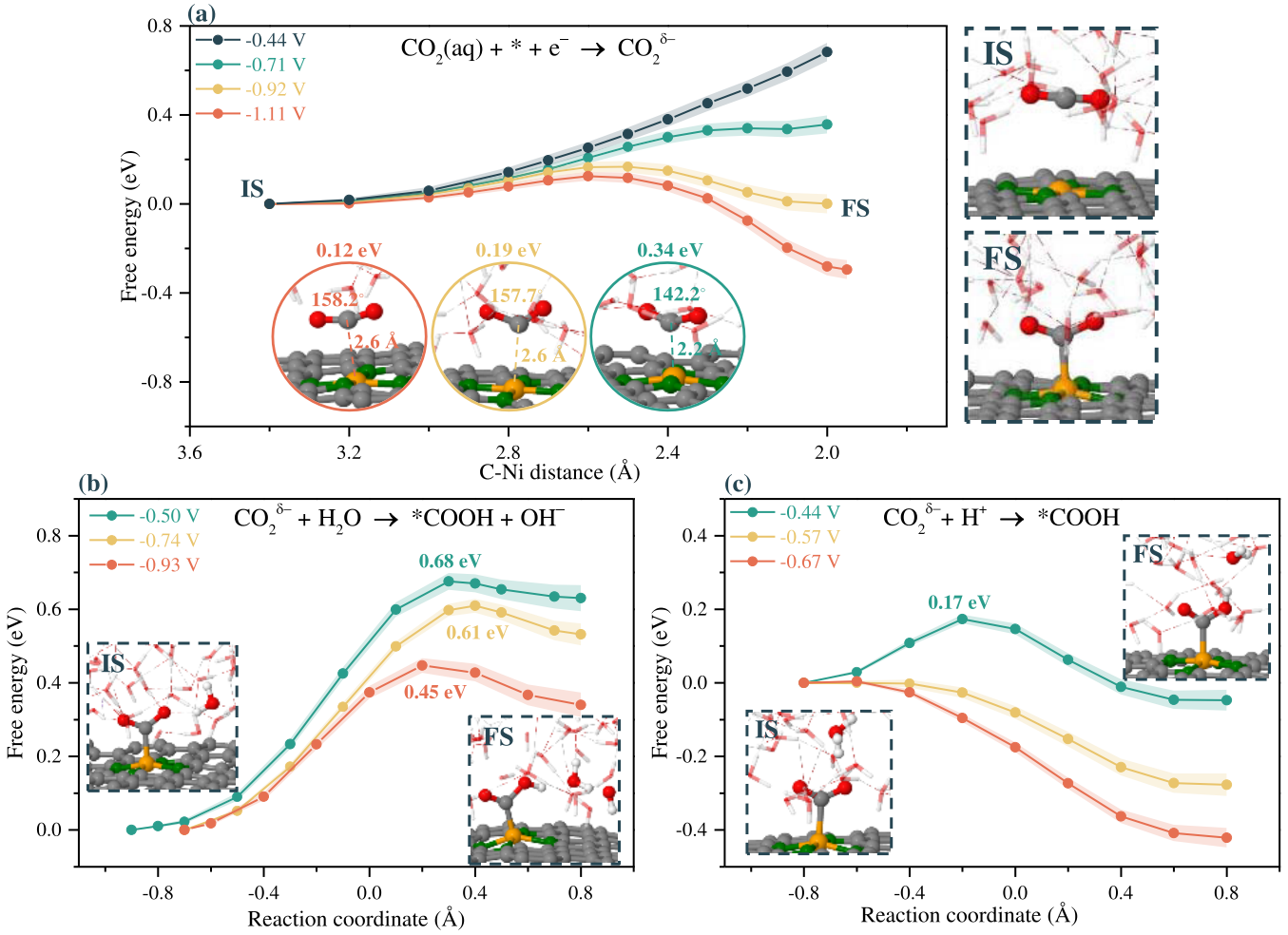

Figure 3. Reaction free energy profiles with error bars for (a) CO_2 adsorption and (b, c) *COOH formation under basic and acidic environment NiN_4@Gra sites under different electrode potentials (*vs* RHE). The shaded regions indicate 95% confidence intervals based on standard errors obtained using the method of block averaging. Propagation of uncertainty within the thermodynamic integration has been accounted for. The insets depict the representative snapshots of the structural evolution during electrochemical steps, such as IS and FS. The corresponding bond distances and barriers of the transition state (TS) change with the applied potential are labeled.

the free energy paths with error estimates on the NiN_4@Gra site under different applied potentials. The reaction energy profiles for the other three sites, NiN_1C_3@Gra, NiN_2C_2@Gra, and NiN_3C_1@Gra, are attached in Figures S1−S3. Here, we consider that the active center is Ni over the catalyst surface throughout this article.[20,21,23] These processes are initiated by CO_2 adsorption for all studied sites. As one can see, the free energy profile for the NiN_4@Gra site rises continually without reaching a free energy minimum when CO_2 approaches the surface at $U = -0.44$ V (*vs* RHE) applied potential (Figure 3a), strongly indicating that the direct activation of CO_2 is rather unfeasible. However, as the electrode potential drops to −0.71 V, the conversion of linear CO_2 to the partially anionic $*CO_2$ intermediate (Figures 3a and 4a,b),[59−61] stabilized by the interfacial electric field,[26,62] is more kinetically and thermodynamically favorable, in which the activation barrier is 0.32 eV. The insets in Figure 3a illustrate the geometric change of the TS where the C−Ni distances increased from 2.2 to 2.6 Å as $U_{RHE} = -0.71$ V changes to −0.92 V; meanwhile, the O-C-O angle, averaged over the last 5 ps from the constrained MD calculation trajectories, stretched from 142.2 to 157.7°. Our results demonstrate that the location of the TS along the reaction coordinate shifted closer to the FS as the applied potential shifts to a more negative value.[55] At the potential of −1.11 V *vs* RHE, the free energy barrier dropped as low as 0.13 ± 0.02 eV, making the path of CO_2 activation be more inclined to convert the IS into the FS with an exothermic reaction energy of −0.25 ± 0.04 eV. The depicted error margins correspond to a 95% confidence interval based on standard errors determined using the method of block averaging and the statistical inefficiency test. Additionally, propagation of uncertainty within the thermodynamic integration has been properly accounted for.[63]

In addition, we find that the TS barrier ($\Delta G^{\ddagger}$) and free energy (ΔG) approximately correlate with U in a linear relationship, which will be discussed in a more detailed way in terms of kinetics later. Compared with CO_2 activation, the conversion of $*CO_2$ to *COOH under basic conditions (Figure 3b) goes through hard processes with all barriers over 0.45 eV, while in the acidic electrolyte, this step apparently involves facile TSs and lower free energy barriers (Figure 3c) at the corresponding applied potential. We further performed constrained MD and thermodynamic integration simulations to explore the conversion of *COOH to *CO on the NiN_4@Gra site. It is shown that the splitting of COOH step is concomitant with CO desorption and formation of H_2O

https://doi.org/10.1021/acscatal.2c02383
ACS Catal. 2022, 12, 11380−11390

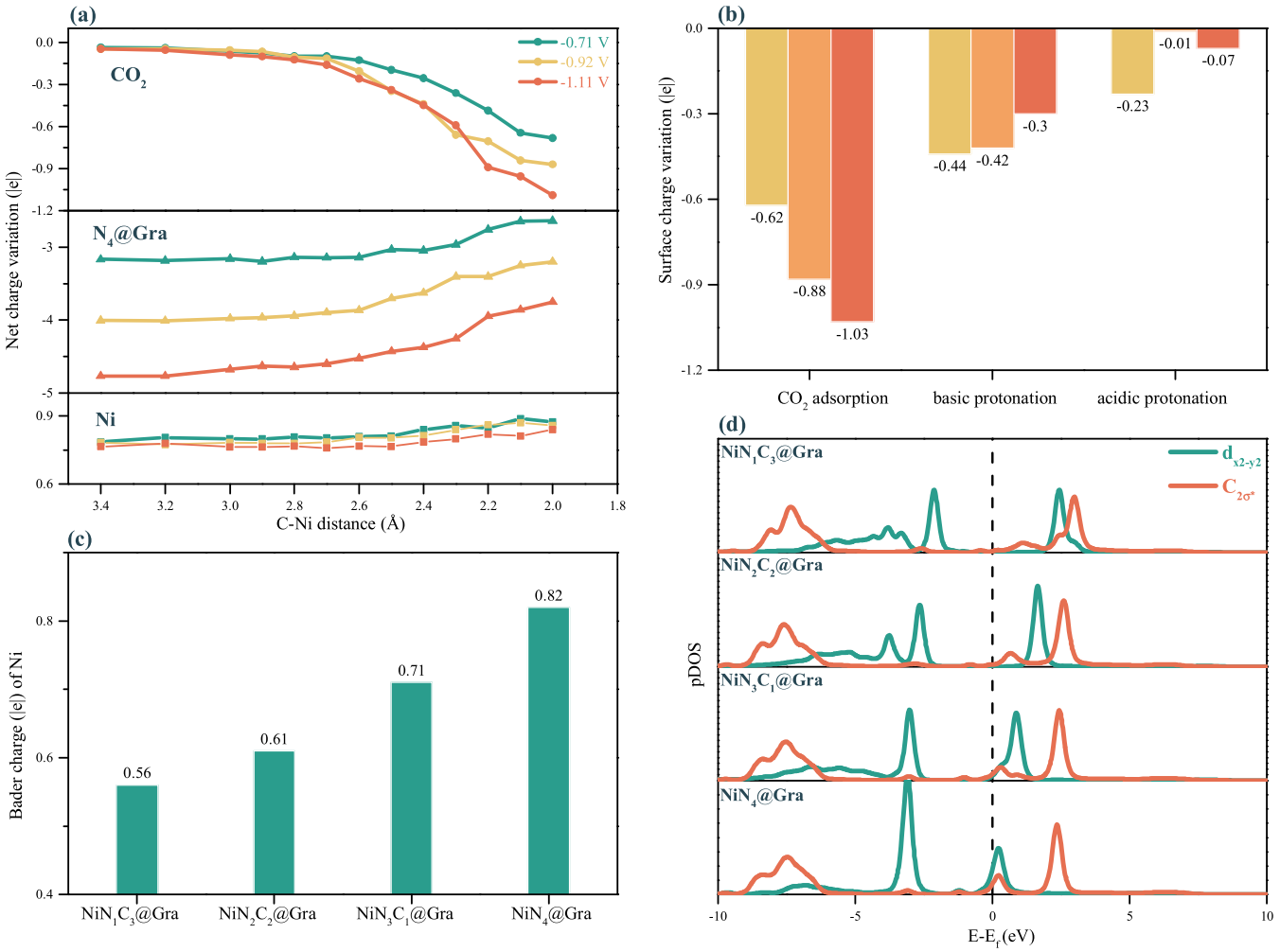

Figure 4. Charge analysis. (a) Bader charge evolution of CO_2, Ni and N_4@Gra during the CO_2 activation process under different applied potentials, averaged from the last 5 ps of total 10 ps constrained MD calculations of Bader charge from each constrained point. (b) Bader charge variation of CO_2 part for three different processes of CO_2 activation, *COOH formation under basic and acidic environment, respectively. (c) Bader charge of Ni center for all studied sites under PZC. (d) Projected density of states (pDOS) of $3d_{x2-y2}$ orbitals for Ni center in all sites and $C_{2\sigma^*}$ orbitals of CO_2.

molecules barrierlessly. Consequently, we concluded that CO_2 activation is the RDS on the NiN_4@Gra electrode in the acidic electrolyte, and while in a basic environment, the protonation of the adsorbed CO_2 to form the *COOH intermediate step is the RDS.

For the other three sites NiN_1C_3@Gra, NiN_2C_2@Gra, and NiN_3C_1@Gra (Figures S1−S3), when it comes to CO_2 adsorption, one might see that NiN_2C_2@Gra has a similar reactivity as NiN_1C_3@Gra at the relevant potentials when it comes to the reaction barrier. NiN_3C_1@Gra and NiN_4@Gra are found to have higher barriers for electrochemical steps than NiN_1C_3@Gra and NiN_2C_2@Gra sites. Specifically, the NiN_4@Gra site is difficult to activate CO_2 at U_{RHE} = −0.44 V (Figure 3a) with the free energy blowing up. Afterward, the following protonation of $*CO_2$−*COOH in both basic and acidic solutions of the other three sites mainly holds the same conclusions, i.e., CO_2 adsorption is the RDS in the acidic environment for all active sites we studied, while it is $*CO_2$ protonation under basic conditions.

To better probe the CO_2 adsorption mechanistic behaviors and the active site structures, charge transfer between CO_2 and the catalyst substrate NiN_4@Gra under different applied potentials, using the trajectory-averaged Bader charge from the last 5 ps of constrained MD simulation of each constrained point, is further analyzed (Figure 4a,b). As expected in Figure 4a, when CO_2 approaches the NiN_4@Gra surface, the net Bader charge shifts negatively to ∼−0.6 |e| when U = −0.71 V *vs* RHE. When U continually drops to −1.11 V, one could see that CO_2 gains more electrons. The remarkable charge transfer manifests the partial reduction nature of the CO_2 chemisorption, which requires a more negative applied potential to take place. We also compared the partial charge transfer nature of CO_2 in all three elementary steps of CO_2 adsorption and $*CO_2$ hydrogenation in both basic and acidic solutions (Figure 4b).

It is worth noting that the hydrogenation step under acidic condition shows a much smaller surface charge variation compared with the CO_2 activation step (Figure 4b), together with the barrierless property (Figure 3c). On the contrary, under basic conditions, the comparatively small partial Bader charge transfer in the hydrogenation step, together with the almost unchanged high barriers (over 0.45 eV, Figure 3b), even when the applied potential decreases evidently, further indicates that the proton uptake from the adjacent water

https://doi.org/10.1021/acscatal.2c02383
ACS Catal. 2022, 12, 11380−11390

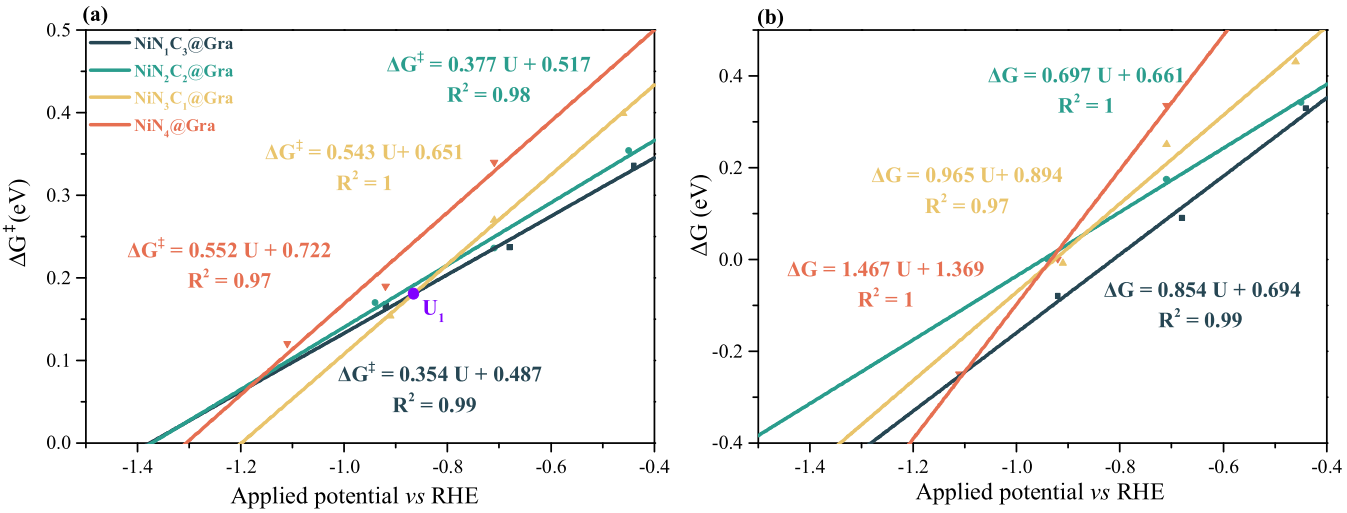

Figure 5. Potential-dependent energetics of CO_2RR. (a) Linear correlation of the CO_2 activation barrier, $\Delta G^{\ddagger}$, *vs* applied potential, U_{RHE}, (b) free energy, ΔG, *vs* U_{RHE} for NiN_1C_3@Gra (black line), NiN_2C_2@Gra (cyan line), NiN_3C_1@Gra (yellow line), and NiN_4@Gra (orange line). The lines represent the fitting relationship, while the light purple circle represents the crossover potential.

molecules keeps relatively harder compared to CO_2 adsorption, evidencing that the magnitude of electrode potential has less impact on the protonation step under alkaline conditions.

In Figure 4a, the net Bader charge of the Ni active center is almost constant at ∼0.75 |e| at −0.71 V and same as that when *U* changed negatively to −0.92 and −1.11 V, suggesting that the active center, Ni, remains almost constant in the reduction process and is just an electron relay during the CO_2 activation, and instead, the graphene matrix is the electron donor when the N_4@Gra charge increased over 0.6 |e| under three different potentials (Figure 4a). A similar phenomenon is reported on the FeN_4@Gra substrate erewhile.[55] This implies that it is the effective surface charge density[20] that drives the charge transfer to CO_2. The "charge capacity" difference for the single Ni site can be ascribed to the charge redistribution between Ni and its coordination sphere, in which enhancing the d−p orbital interaction between the active center and adsorbate is one of the main ideas. As a matter of fact, many previous experimental investigations had evidenced that the adjustment of the active center, such as, the axial ligand effect and coordination environment tuning, would give rise to stability variations of electrocatalysts, inducing catalytic performance improvement.[64−66]

To understand the reactivity difference of the NiN_nC_{4-n}@Gra catalyst toward the electrocatalytic CO_2RR, static density functional theory (DFT) calculations are carried out to reveal the Bader charge of Ni under PZC (Figure 4c) and projected density of states (pDOS) of $3d_{x2-y2}$ (Ni) orbitals and $C_{2\sigma}$* orbitals of CO_2 at U_{RHE} = −0.92 V in different Ni-N structures (Figure 4d). As shown in Figure 4c, the oxidation state of Ni is increasingly higher, as the coordinated N number increases, indicating the occupation of the $3d_{x2-y2}$ orbital (HOMO) of the center,[24] which is more inclined to overlap with the $C_{2\sigma}$* (LUMO) orbital of CO_2, decreasing. In addition, Figure 4d displays that some hybridized electronic states occur above the Fermi level when CO_2 approaches the electrode, leading to that the antibonding states of the Ni−C bond are relatively less occupied, as the number of dopant N increases, so that the Ni−C bonding is weakened, which is consistent with earlier observations of the reactivity variation trend of the CuN_nC_{4-n}@Gra-catalyzed oxygen reduction reaction (ORR).[39] For these reasons, CO_2 activation over the NiN_4@Gra surface undergoes the hardest process compared with other sites at the respective applied potential.

Potential-Dependent Kinetics of the CO_2RR. To investigate the effect of potential on the aforementioned CO_2 activation behaviors from the aspects of kinetics, we further plot the correlation between the reaction barrier of CO_2 activation ($\Delta G^{\ddagger}$) and free energy (ΔG) with the electrode potential in Figure 5, and linear relationships could be approximately obtained for all the studied sites. The slope denotes the magnitude of the potential dependence of CO_2 activation. The different values of the slope correspond to the effects from several factors such as the amount of the transferred electrons upon the adsorption and the solvation from the solvent water molecules at the electrochemical interface and the catalyst electronic structure,[67] while the intercept corresponds to the energetics at zero potential. Due to the deviations in the slope, a crossover point, labeled in light purple, occurs at potential U_1 = −0.87 V (Figure 5a). As the figure demonstrates, the fitting solid lines of NiN_1C_3@Gra (in black) and NiN_2C_2@Gra (in cyan) almost overlapped one another, indicating that they characterized approximate reactivity. In the lower electrode potential regime (U_{RHE} > U_1), NiN_1C_3@Gra and NiN_2C_2@Gra are more active than NiN_3C_1@Gra (in orange) and NiN_4@Gra (in yellow). Then, as the electrode continuously drops to the range of −1.2 V < U_{RHE} < U_1, NiN_3C_1@Gra begins to enter the stage of catalysis and govern CO_2 activation, whereas at U_{RHE} < −1.2 V, the catalytic performance of NiN_4@Gra would overwhelm that of NiN_1C_3@Gra and NiN_2C_2@Gra sites. However, as Figure 5a demonstrates, when U_{RHE} < −1.2 V, CO_2 adsorption on all the studied sites is almost barrierless (less than 0.1 eV). We further identified linear scaling relationships between the reaction free energy (ΔG) of CO_2 adsorption and the applied potential (Figure 5b), of which the slope is not as simple as 1 eV per volt, as suggested by the traditional CHE model. For NiN_1C_3@Gra, NiN_2C_2@Gra, and NiN_3C_1@Gra, the slope is less than 1 eV per volt, which is consistent with the small charge transfer from the substrate to CO_2 upon adsorption, as shown in Table S3. For NiN_4@Gra, the slop is significantly

https://doi.org/10.1021/acscatal.2c02383
ACS Catal. 2022, 12, 11380−11390

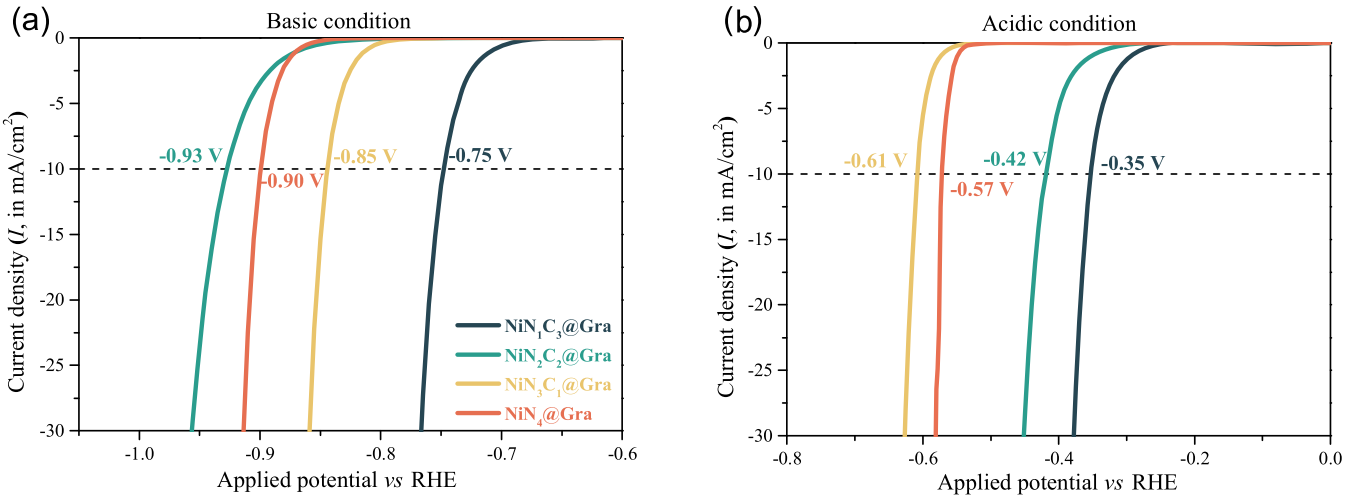

Figure 6. Calculated partial current densities for CO evolution during CO_2 reduction under (a) basic and (b) acidic conditions on NiN_1C_3@Gra (black line), NiN_2C_2@Gra (cyan line), NiN_3C_1@Gra (yellow line), and NiN_4@Gra (orange line). The assumed activity coefficient f is set to 0.1 for all systems.

larger than 1 eV per volt owing to the higher charge transfer for CO_2 adsorption and the solvation effect on the free energetics.[55]

Next, we analyzed the kinetics of CO production by applying the LPD-K model and linear fitting equations of $\Delta G^{\ddagger}$ and ΔG *vs* U_{RHE} (Figure 5), together with $\Delta G_p^{\#}(U)$ *vs* U_{RHE} (Table S4) for NiN_1C_3@Gra, NiN_2C_2@Gra, NiN_3C_1@Gra, and NiN_4@Gra sites. By adopting an empirical parameter of 0.1 for the activity coefficient, f, we obtain the current density changed as a function of the applied potential shown in Figure 6 for the CO evolution under basic and acidic conditions. Details of calculating the $I-U$ curves are attached in Supporting Note 1. Experimentally, the onset potential is typically defined to be the applied voltage achieving 10 mA·cm^{-2} for the catalyst. As shown in Figure 6a, the NiN_1C_3@Gra site shows the best activity of the CO_2RR and the predicted onset potential is −0.75 V under basic conditions. NiN_3C_1@Gra shows a U_{onset} of −0.85 V, agreeing very well with the experimental reports, −0.89 V.[9] For the NiN_4@Gra site and NiN_2C_2@Gra, U_{onset} is estimated to be −0.90 and −0.85 V, respectively. Overall, the predicted U_{onset} for all sites lies in the reasonably minimal range form −0.75 to −0.93 V to realize 10 mA·cm^{-2} current density, agreeing very well with the experimental observations, in which the coordinatively unsaturated Ni SAC maintains a broad catalysis potential window from −0.53 to −1.03 V.[8,24,30] In contrast, we notice in Figure 6b that the corresponding U_{onset} under acidic conditions for all four sites also exhibits good performance in the the CO_2RR in regard to activity and durability, echoing the earlier experimental research that suggests the current density of Ni-CNT-CC under acidic conditions, which was obviously higher than that under basic conditions,[11] although the low CO_2RR activity usually arises from the undesired competing side reactions, i.e., hydrogen evolution reaction (HER). What is more is that we noted that such a predicted U_{onset} result on NiN_3C_1@Gra agrees best with the experiment,[9] while the other three U_{onset} values are acceptable in contrast with the reported MNC@Gra catalyst in catalyzing the CO_2RR in the previous literature,[12] in which the CO faradaic efficiencies on the NiNC@Gra electrode rival those of FeNC@Gra, even showing higher efficiency than Au- and Ag-based catalysts.

We have also performed sensitivity analysis to testify the impact of f on the potential-dependent kinetics. By adopting 0.01 and 0.5 values for f, the corresponding $I-U$ plots can be obtained in Figure S4. It is shown that with the f decreasing from 0.1 to 0.01, the predicted U_{onset} only slightly shifts to less than 0.05 V for all the sites. Also, increasing f 5 times, the predicted U_{onset} variations remain virtually unchanged. These results suggested that the observed potential-dependent kinetics are not significantly affected by the value of f and the decided onset potentials are mainly determined by the free energetics of both the adsorption and protonation steps, which are significantly potential-dependent. In fact, it has to be noted that experimental determination of the actual active site playing the critical role in the CO_2RR is difficult, in which the coordination number (CN) of Ni is controversial.[8,9,40] By the implementation of the constructed LPD-K model, we predict all the four studied sites to be indispensable to construct the practical observed broad potential window[8] and to achieve the overall observed CO current increases one after another, to maintain the high level but maybe in different proportions. What is more is that by precisely manipulating the CN portions, we believe that it is possible to maximize CO production of the desired site.

CONCLUSIONS

In summary, we have investigated the potential-dependent free energetics of the CO_2RR on single-nickel atom catalysts on a nitrogen-doped graphene support using ab initio molecular dynamics simulations with fully explicit solvation. We have split the first proton-coupled electron transfer step into CO_2 adsorption and protonation steps, where the former mainly accounts for the electron transfer. We have found that the rate-determining step under acidic conditions is CO_2 adsorption and under basic conditions, it is the first protonation step. We have further shown that the Langmuir adsorption model-derived potential-dependent kinetics in regard to thermodynamics provided a fundamental insight into understanding electrochemical processes. Our formulation provides the prediction of the potential-dependent kinetics of the CO_2RR on NiN_nC_{4-n}@Gra substrates in an explicit solvation model. By the adoption of the proposed kinetic model, we predict the

https://doi.org/10.1021/acscatal.2c02383
ACS Catal. 2022, 12, 11380−11390

onset potentials of the CO_2RR, which are comparable with experimental observations. Our findings reveal that a relatively low N content in the proximity of Ni active centers can lead to higher CO_2RR activity and selectivity as compared to the original NiN_4 site.

The present methodology based on the potential-dependent Langmuir adsorption model to understand the kinetics is distinctly different from the traditional free energy descriptions of electrochemistry, in which the potential surface proceeds keeping a constant number of electrons. Our formulation arises naturally from equilibrated adsorbate coverage obeying the Langmuir isotherm and can be determined by the applied potential. This methodology can be relevant not only for other SACs or materials with evident adsorbate−field interactions but also for other electrochemical processes in which the adsorbate coverage is decisive. We believe that our findings and the methodology presented here will inspire rational design of the active sites and the optimization of catalytic conditions for CO_2RR catalysts at the atomic scale and more importantly guide the identification of the actual sites playing the critical role in CO evolution in experimentally synthesized SACs in the future.

■ ASSOCIATED CONTENT

Supporting Information

The Supporting Information is available free of charge at https://pubs.acs.org/doi/10.1021/acscatal.2c02383.

Reaction free energy profiles of CO_2 adsorption and *COOH formation on NiN_nC_{4-n}@Gra (n = 2−4); snapshots for the hydrogen evolution reaction during the constrained MD simulations on NiN_nC_{4-n}@Gra (n = 1−4); and supplementary notes for calculating the kinetics of the CO_2RR (PDF)

■ AUTHOR INFORMATION

Corresponding Author

Yang-Gang Wang − *Shenzhen Key Laboratory of Energy Chemistry, Southern University of Science and Technology, Shenzhen 518055, China; Department of Chemistry and Guangdong Provincial Key Laboratory of Catalysis, Southern University of Science and Technology, Shenzhen 518055 Guangdong, China;* orcid.org/0000-0002-0582-0855; Email: wangyg@sustech.edu.cn

Authors

Hongyan Zhao − *Shenzhen Key Laboratory of Energy Chemistry, Southern University of Science and Technology, Shenzhen 518055, China; Department of Chemistry and Guangdong Provincial Key Laboratory of Catalysis, Southern University of Science and Technology, Shenzhen 518055 Guangdong, China*

Hao Cao − *Shenzhen Key Laboratory of Energy Chemistry, Southern University of Science and Technology, Shenzhen 518055, China; Department of Chemistry and Guangdong Provincial Key Laboratory of Catalysis, Southern University of Science and Technology, Shenzhen 518055 Guangdong, China*

Zisheng Zhang − *Department of Chemistry and Biochemistry, University of California, Los Angeles, Los Angeles, California 90095, United States;* orcid.org/0000-0002-4370-4038

Complete contact information is available at: https://pubs.acs.org/10.1021/acscatal.2c02383

Notes

The authors declare no competing financial interest.

■ ACKNOWLEDGMENTS

This work is financially supported by the NSFC (No. 22022504) of China, Guangdong "Pearl River" Talent Plan (No. 2019QN01L353), Higher Education Innovation Strong School Project of Guangdong Province of China (2020KTSCX122), Guangdong Provincial Key Laboratory of Catalysis (No. 2020B121201002), and the Shenzhen Science and Technology Innovation Committee (Grant No. ZDSYS20200421111001787). The computational resources are also provided by the Center for Computational Science and Engineering at the Southern University of Science and Technology (SUSTech) and the CHEM high-performance computing cluster (CHEM-HPC) located at the Department of Chemistry, SUSTech.

■ REFERENCES

(1) Duan, X. C.; Xu, J. T.; Wei, Z. X.; Ma, J. M.; Guo, S. J.; Wang, S. Y.; Liu, H. K.; Dou, S. X. Metal-Free Carbon Materials for CO_2 Electrochemical Reduction. *Adv. Mater.* **2017**, *29*, No. 1701784.

(2) Hoffert, M. I.; Caldeira, K.; Benford, G.; Criswell, D. R.; Green, C.; Herzog, H.; Jain, A. K.; Kheshgi, H. S.; Lackner, K. S.; Lewis, J. S.; Lightfoot, H. D.; Manheimer, W.; Mankins, J. C.; Mauel, M. E.; Perkins, L. J.; Schlesinger, M. E.; Volk, T.; Wigley, T. M. L. Advanced technology paths to global climate stability: Energy for a greenhouse planet. *Science* **2002**, *298*, 981−987.

(3) Centi, G.; Quadrelli, E. A.; Perathoner, S. Catalysis for CO_2 conversion: a key technology for rapid introduction of renewable energy in the value chain of chemical industries. *Energy Environ. Sci.* **2013**, *6*, 1711−1731.

(4) Qiao, J. L.; Liu, Y. Y.; Hong, F.; Zhang, J. J. A review of catalysts for the electroreduction of carbon dioxide to produce low-carbon fuels. *Chem. Soc. Rev.* **2014**, *43*, 631−675.

(5) Ross, M. B.; De Luna, P.; Li, Y. F.; Dinh, C. T.; Kim, D.; Yang, P.; Sargent, E. H. Designing materials for electrochemical carbon dioxide recycling. *Nat. Catal.* **2019**, *2*, 648−658.

(6) Zhu, D. D.; Liu, J. L.; Qiao, S. Z. Recent Advances in Inorganic Heterogeneous Electrocatalysts for Reduction of Carbon Dioxide. *Adv. Mater.* **2016**, *28*, 3423−3452.

(7) Qiao, B. T.; Wang, A. Q.; Yang, X. F.; Allard, L. F.; Jiang, Z.; Cui, Y. T.; Liu, J. Y.; Li, J.; Zhang, T. Single-atom catalysis of CO oxidation using Pt-1/FeOx. *Nat. Chem.* **2011**, *3*, 634−641.

(8) Yan, C. C.; Li, H. B.; Ye, Y. F.; Wu, H. H.; Cai, F.; Si, R.; Xiao, J. P.; Miao, S.; Xie, S. H.; Yang, F.; Li, Y. S.; Wang, G. X.; Bao, X. H. Coordinatively unsaturated nickel-nitrogen sites towards selective and high-rate CO_2 electroreduction. *Energy Environ. Sci.* **2018**, *11*, 1204−1210.

(9) Zhao, C. M.; Dai, X. Y.; Yao, T.; Chen, W. X.; Wang, X. Q.; Wang, J.; Yang, J.; Wei, S. Q.; Wu, Y. E.; Li, Y. D. Ionic Exchange of Metal Organic Frameworks to Access Single Nickel Sites for Efficient Electroreduction of CO_2. *J. Am. Chem. Soc.* **2017**, *139*, 8078−8081.

(10) Su, P.; Iwase, K.; Nakanishi, S.; Hashimoto, K.; Kamiya, K. Nickel-Nitrogen-Modified Graphene: An Efficient Electrocatalyst for the Reduction of Carbon Dioxide to Carbon Monoxide. *Small* **2016**, *12*, 6083−6089.

(11) Liu, S.; Yang, H. B.; Hung, S. F.; Ding, J.; Cai, W. Z.; Liu, L. H.; Gao, J. J.; Li, X. N.; Ren, X. Y.; Kuang, Z. C.; Huang, Y. Q.; Zhang, T.; Liu, B. Elucidating the Electrocatalytic CO_2 Reduction Reaction over a Model Single-Atom Nickel Catalyst. *Angew. Chem., Int. Ed.* **2020**, *59*, 798−803.

(12) Ju, W.; Bagger, A.; Hao, G. P.; Varela, A. S.; Sinev, I.; Bon, V.; Roldan Cuenya, B.; Kaskel, S.; Rossmeisl, J.; Strasser, P. Understanding activity and selectivity of metal-nitrogen-doped carbon catalysts for electrochemical reduction of CO_2. *Nat. Commun.* **2017**, *8*, No. 944.

(13) Wuttig, A.; Yaguchi, M.; Motobayashi, K.; Osawa, M.; Surendranath, Y. Inhibited proton transfer enhances Au-catalyzed CO_2-to-fuels selectivity. *Proc. Natl. Acad. Sci. U.S.A.* **2016**, *113*, E4585−E4593.
(14) Verma, S.; Hamasaki, Y.; Kim, C.; Huang, W. X.; Lu, S.; Jhong, H. R. M.; Gewirth, A. A.; Fujigaya, T.; Nakashima, N.; Kenis, P. J. A. Insights into the Low Overpotential Electroreduction of CO_2 to CO on a Supported Gold Catalyst in an Alkaline Flow Electrolyzer. *ACS Energy Lett.* **2018**, *3*, 193−198.
(15) Varela, A. S.; Kroschel, M.; Leonard, N. D.; Ju, W.; Steinberg, J.; Bagger, A.; Rossmeisl, J.; Strasser, P. pH Effects on the Selectivity of the Electrocatalytic CO_2 Reduction on Graphene-Embedded Fe-N-C Motifs: Bridging Concepts between Molecular Homogeneous and Solid-State Heterogeneous Catalysis. *ACS Energy Lett.* **2018**, *3*, 812−817.
(16) Prslja, P.; Lopez, N. Stability and Redispersion of Ni Nanoparticles Supported on N-Doped Carbons for the CO_2 Electrochemical Reduction. *ACS Catal.* **2021**, *11*, 88−94.
(17) Dunwell, M.; Lu, Q.; Heyes, J. M.; Rosen, J.; Chen, J. G. G.; Yan, Y. S.; Jiao, F.; Xu, B. J. The Central Role of Bicarbonate in the Electrochemical Reduction of Carbon Dioxide on Gold. *J. Am. Chem. Soc.* **2017**, *139*, 3774−3783.
(18) Hansen, H. A.; Varley, J. B.; Peterson, A. A.; Norskov, J. K. Understanding Trends in the Electrocatalytic Activity of Metals and Enzymes for CO_2 Reduction to CO. *J. Phys. Chem. Lett.* **2013**, *4*, 388−392.
(19) Chen, L. D.; Urushihara, M.; Chan, K. R.; Norskov, J. K. Electric Field Effects in Electrochemical CO_2 Reduction. *ACS Catal* **2016**, *6*, 7133−7139.
(20) Zhao, X. H.; Liu, Y. Y. Unveiling the Active Structure of Single Nickel Atom Catalysis: Critical Roles of Charge Capacity and Hydrogen Bonding. *J. Am. Chem. Soc.* **2020**, *142*, 5773−5777.
(21) Li, X. G.; Bi, W. T.; Chen, M. L.; Sun, Y. X.; Ju, H. X.; Yan, W. S.; Zhu, J. F.; Wu, X. J.; Chu, W. S.; Wu, C. Z.; Xie, Y. Exclusive Ni-N-4 Sites Realize Near-Unity CO Selectivity for Electrochemical CO_2 Reduction. *J. Am. Chem. Soc.* **2017**, *139*, 14889−14892.
(22) Vijay, S.; Ju, W.; Bruckner, S.; Tsang, S. C.; Strasser, P.; Chan, K. R. Unified mechanistic understanding of CO_2 reduction to CO on transition metal and single atom catalysts. *Nat. Catal.* **2021**, *4*, 1024−1031.
(23) Hossain, M. D.; Huang, Y. F.; Yu, T. H.; Goddard, W. A.; Luo, Z. T. Reaction mechanism and kinetics for CO_2 reduction on nickel single atom catalysts from quantum mechanics. *Nat. Commun.* **2020**, *11*, No. 2256.
(24) Yang, H. B.; Hung, S. F.; Liu, S.; Yuan, K. D.; Miao, S.; Zhang, L. P.; Huang, X.; Wang, H. Y.; Cai, W. Z.; Chen, R.; Gao, J. J.; Yang, X. F.; Chen, W.; Huang, Y. Q.; Chen, H. M.; Li, C. M.; Zhang, T.; Liu, B. Atomically dispersed Ni(i) as the active site for electrochemical CO_2 reduction. *Nat. Energy* **2018**, *3*, 140−147.
(25) Nørskov, J. K.; Rossmeisl, J.; Logadottir, A.; Lindqvist, L.; Kitchin, J. R.; Bligaard, T.; Jonsson, H. Origin of the overpotential for oxygen reduction at a fuel-cell cathode. *J. Phys. Chem. B* **2004**, *108*, 17886−17892.
(26) Vijay, S.; Gauthier, J. A.; Heenen, H. H.; Bukas, V. J.; Kristoffersen, H. H.; Chan, K. R. Dipole-Field Interactions Determine the CO_2 Reduction Activity of 2D Fe-N-C Single-Atom Catalysts. *ACS Catal.* **2020**, *10*, 7826−7835.
(27) Filhol, J. S.; Neurock, M. Elucidation of the electrochemical activation of water over Pd by first principles. *Angew. Chem., Int. Ed.* **2006**, *45*, 402−406.
(28) Li, C. Y.; Le, J. B.; Wang, Y. H.; Chen, S.; Yang, Z. L.; Li, J. F.; Cheng, J.; Tian, Z. Q. In situ probing electrified interfacial water structures at atomically flat surfaces. *Nat. Mater.* **2019**, *18*, 697−701.
(29) Le, J. B.; Fan, Q. Y.; Li, J. Q.; Cheng, J. Molecular origin of negative component of Helmholtz capacitance at electrified Pt(111)/water interface. *Sci. Adv.* **2020**, *6*, No. eabb1219.
(30) Jiang, K.; Siahrostami, S.; Zheng, T. T.; Hu, Y. F.; Hwang, S.; Stavitski, E.; Peng, Y. D.; Dynes, J.; Gangisetty, M.; Su, D.; Attenkofer, K.; Wang, H. T. Isolated Ni single atoms in graphene nanosheets for high-performance CO_2 reduction. *Energy Environ. Sci.* **2018**, *11*, 893−903.
(31) Perdew, J. P.; Burke, K.; Ernzerhof, M. Generalized gradient approximation made simple. *Phys. Rev. Lett.* **1996**, *77*, 3865−3868.
(32) Kresse, G.; Furthmuller, J. Efficient iterative schemes for ab initio total-energy calculations using a plane-wave basis set. *Phys. Rev. B* **1996**, *54*, 11169−11186.
(33) Kresse, G.; Furthmuller, J. Efficiency of ab-initio total energy calculations for metals and semiconductors using a plane-wave basis set. *Comput. Mater. Sci.* **1996**, *6*, 15−50.
(34) Perdew, J. P.; Chevary, J. A.; Vosko, S. H.; Jackson, K. A.; Pederson, M. R.; Singh, D. J.; Fiolhais, C. Atoms, molecules, solids, and surfaces: Applications of the generalized gradient approximation for exchange and correlation. *Phys. Rev. B* **1992**, *46*, 6671−6687.
(35) Blöchl, P. E. Projector augmented-wave method. *Phys. Rev. B* **1994**, *50*, 17953−17979.
(36) Li, Y. G.; Zhou, W.; Wang, H. L.; Xie, L. M.; Liang, Y. Y.; Wei, F.; Idrobo, J. C.; Pennycook, S. J.; Dai, H. J. An oxygen reduction electrocatalyst based on carbon nanotube-graphene complexes. *Nat. Nanotechnol.* **2012**, *7*, 394−400.
(37) Jiang, K.; Siahrostami, S.; Akey, A. J.; Li, Y. B.; Lu, Z. Y.; Lattimer, J.; Hu, Y. F.; Stokes, C.; Gangishetty, M.; Chen, G. X.; Zhou, Y. W.; Hill, W.; Cai, W. B.; Bell, D.; Chan, K. R.; Norskov, J. K.; Cui, Y.; Wang, H. T. Transition-Metal Single Atoms in a Graphene Shell as Active Centers for Highly Efficient Artificial Photosynthesis. *Chem* **2017**, *3*, 950−960.
(38) Sharma, P. P.; Wu, J. J.; Yadav, R. M.; Liu, M. J.; Wright, C. J.; Tiwary, C. S.; Yakobson, B. I.; Lou, J.; Ajayan, P. M.; Zhou, X. D. Nitrogen-Doped Carbon Nanotube Arrays for High-Efficiency Electrochemical Reduction of CO_2: On the Understanding of Defects, Defect Density, and Selectivity. *Angew. Chem., Int. Ed.* **2015**, *54*, 13701−13705.
(39) Wu, H. H.; Li, H. B.; Zhao, X. F.; Liu, Q. F.; Wang, J.; Xiao, J. P.; Xie, S. H.; Si, R.; Yang, F.; Miao, S.; Guo, X. G.; Wang, G. X.; Bao, X. H. Highly doped and exposed Cu(I)-N active sites within graphene towards efficient oxygen reduction for zinc-air batteries. *Energy Environ. Sci.* **2016**, *9*, 3736−3745.
(40) Fei, H. L.; Dong, J. C.; Feng, Y. X.; Allen, C. S.; Wan, C. Z.; Volosskiy, B.; Li, M. F.; Zhao, Z. P.; Wang, Y. L.; Sun, H. T.; An, P. F.; Chen, W. X.; Guo, Z. Y.; Lee, C.; Chen, D. L.; Shakir, I.; Liu, M. J.; Hu, T. D.; Li, Y. D.; Kirkland, A. I.; Duan, X. F.; Huang, Y. General synthesis and definitive structural identification of MN4C4 single-atom catalysts with tunable electrocatalytic activities. *Nat. Catal.* **2018**, *1*, 63−72.
(41) VandeVondele, J.; Krack, M.; Mohamed, F.; Parrinello, M.; Chassaing, T.; Hutter, J. QUICKSTEP: Fast and accurate density functional calculations using a mixed Gaussian and plane waves approach. *Comput. Phys. Commun.* **2005**, *167*, 103−128.
(42) Hartwigsen, C.; Goedecker, S.; Hutter, J. Relativistic separable dual-space Gaussian pseudopotentials from H to Rn. *Phys. Rev. B* **1998**, *58*, 3641−3662.
(43) Goedecker, S.; Teter, M.; Hutter, J. Separable dual-space Gaussian pseudopotentials. *Phys. Rev. B* **1996**, *54*, 1703−1710.
(44) Lippert, G.; Hutter, J.; Parrinello, M. The Gaussian and augmented-plane-wave density functional method for ab initio molecular dynamics simulations. *Theor. Chem. Acc.* **1999**, *103*, 124−140.
(45) VandeVondele, J.; Hutter, J. Gaussian basis sets for accurate calculations on molecular systems in gas and condensed phases. *J. Chem. Phys.* **2007**, *127*, No. 114105.
(46) Grimme, S.; Antony, J.; Ehrlich, S.; Krieg, H. A consistent and accurate ab initio parametrization of density functional dispersion correction (DFT-D) for the 94 elements H-Pu. *J. Chem. Phys.* **2010**, *132*, No. 154104.
(47) Nosé, S. A Unified Formulation of the Constant Temperature Molecular-Dynamics Methods. *J. Chem. Phys.* **1984**, *81*, 511−519.
(48) Hoover, W. G. Canonical Dynamics - Equilibrium Phase-Space Distributions. *Phys. Rev. A* **1985**, *31*, 1695−1697.

https://doi.org/10.1021/acscatal.2c02383
ACS Catal. 2022, 12, 11380−11390

(49) Carter, E. A.; Ciccotti, G.; Hynes, J. T.; Kapral, R. Constrained Reaction Coordinate Dynamics for the Simulation of Rare Events. *Chem. Phys. Lett.* **1989**, *156*, 472−477.
(50) Sprik, M.; Ciccotti, G. Free energy from constrained molecular dynamics. *J. Chem. Phys.* **1998**, *109*, 7737−7744.
(51) Chipot, C.; Pohorille, A.*Free Energy Calculations: Theory and Applications in Chemistry and Biology*; Springer Series in Chemical Physics; Springer, 2007; Vol. *86*, p 517.
(52) Gauthier, J. A.; Dickens, C. F.; Heenen, H. H.; Vijay, S.; Ringe, S.; Chan, K. Unified Approach to Implicit and Explicit Solvent Simulations of Electrochemical Reaction Energetics. *J. Chem. Theory Comput.* **2019**, *15*, 6895−6906.
(53) Chen, J.; Li, C.; Shi, G. Graphene Materials for Electrochemical Capacitors. *J. Phys. Chem. Lett.* **2013**, *4*, 1244−1253.
(54) Choi, C. H.; Lim, H.-K.; Chung, M. W.; Chon, G.; Ranjbar Sahraie, N.; Altin, A.; Sougrati, M.-T.; Stievano, L.; Oh, H. S.; Park, E. S.; Luo, F.; Strasser, P.; Dražić, G.; Mayrhofer, K. J. J.; Kim, H.; Jaouen, F. The Achilles' heel of iron-based catalysts during oxygen reduction in an acidic medium. *Energy Environ. Sci.* **2018**, *11*, 3176−3182.
(55) Cao, H.; Zhang, Z. S.; Chen, J. W.; Wang, Y. G. Potential-Dependent Free Energy Relationship in Interpreting theElectrochemical Performance of CO(2)Reduction on Single AtomCatalysts br. *ACS Catal.* **2022**, *12*, 6606−6617.
(56) Chan, K. R.; Norskov, J. K. Electrochemical Barriers Made Simple. *J. Phys. Chem. Lett.* **2015**, *6*, 2663−2668.
(57) Rossmeisl, J.; Skulason, E.; Bjorketun, M. E.; Tripkovic, V.; Norskov, J. K. Modeling the electrified solid-liquid interface. *Chem. Phys. Lett.* **2008**, *466*, 68−71.
(58) Li, Y.; Adli, N. M.; Shan, W. T.; Wang, M. Y.; Zachman, M. J.; Hwang, S.; Tabassum, H.; Karakalos, S.; Feng, Z. X.; Wang, G. F.; Li, Y. C.; Wu, G. Atomically dispersed single Ni site catalysts for high-efficiency CO_2 electroreduction at industrial-level current densities. *Energy Environ. Sci.* **2022**, *15*, 2108−2119.
(59) Dunwell, M.; Luc, W.; Yan, Y. S.; Jiao, F.; Xu, B. J. Understanding Surface-Mediated Electrochemical Reactions: CO_2 Reduction and Beyond. *ACS Catal.* **2018**, *8*, 8121−8129.
(60) Gauthier, J. A.; Fields, M.; Bajdich, M.; Chen, L. D.; Sandberg, R. B.; Chan, K.; Norskov, J. K. Facile Electron Transfer to CO_2 during Adsorption at MetallSolution Interface. *J. Phys. Chem. C* **2019**, *123*, 29278−29283.
(61) Li, J. J.; Liu, J.; Yang, B. Insights into the adsorption/desorption of CO_2 and CO on single-atom Fe-nitrogen-graphene catalyst under electrochemical environment. *J. Energy Chem.* **2021**, *53*, 20−25.
(62) Ringe, S.; Morales-Guio, C. G.; Chen, L. D.; Fields, M.; Jaramillo, T. F.; Hahn, C.; Chan, K. Double layer charging driven carbon dioxide adsorption limits the rate of electrochemical carbon dioxide reduction on Gold. *Nat. Commun.* **2020**, *11*, No. 33.
(63) Kronberg, R.; Lappalainen, H.; Laasonen, K. Revisiting the Volmer-Heyrovsky mechanism of hydrogen evolution on a nitrogen doped carbon nanotube: constrained molecular dynamics versus the nudged elastic band method. *Phys. Chem. Chem. Phys.* **2020**, *22*, 10536−10549.
(64) Wang, F. T.; Zhou, Y. P.; Lin, S.; Yang, L. J.; Hu, Z.; Xie, D. Q. Axial ligand effect on the stability of Fe-N-C electrocatalysts for acidic oxygen reduction reaction. *Nano Energy* **2020**, *78*, No. 105128.
(65) Wang, Y.; Tang, Y. J.; Zhou, K. Self-Adjusting Activity Induced by Intrinsic Reaction Intermediate in Fe-N-C Single-Atom Catalysts. *J. Am. Chem. Soc.* **2019**, *141*, 14115−14119.
(66) Jia, Q.; Ramaswamy, N.; Hafiz, H.; Tylus, U.; Strickland, K.; Wu, G.; Barbiellini, B.; Bansil, A.; Holby, E. F.; Zelenay, P.; Mukerjee, S. Experimental Observation of Redox-Induced Fe-N Switching Behavior as a Determinant Role for Oxygen Reduction Activity. *ACS Nano* **2015**, *9*, 12496−12505.
(67) Choi, C.; Gu, G. H.; Noh, J.; Park, H. S.; Jung, Y. S. Understanding potential-dependent competition between electrocatalytic dinitrogen and proton reduction reactions. *Nat. Commun.* **2021**, *12*, No. 4543.

https://doi.org/10.1021/acscatal.2c02383
ACS Catal. 2022, 12, 11380−11390